Global inundation dynamics inferred from multiple satellite observations, 1993–2000

C. Prigent,[1] F. Papa,[2] F. Aires,[3] W. B. Rossow,[4] and E. Matthews[4]

[1]   Wetlands and surface waters are recognized to play important roles in climate, hydrologic and biogeochemical cycles, and availability of water resources. Until now, quantitative, global time series of spatial and temporal dynamics of inundation have been unavailable. This study presents the first global estimate of monthly inundated areas for 1993–2000. The data set is derived from a multisatellite method employing passive microwave land surface emissivities calculated from SSM/I and ISCCP observations, ERS scatterometer responses, and AVHRR visible and near-infrared reflectances. The satellite data are used to calculate inundated fractions of equal area grid cells ($0.25° \times 0.25°$ at the equator), taking into account the contribution of vegetation to the passive microwave signal. Global inundated area varies from a maximum of 5.86×10^6 km^2 (average for 1993–2000) to a mean minimum of 2.12×10^6 km^2. These values are considered consistent with existing independent, static inventories. The new multisatellite estimates also show good agreement with regional high-resolution SAR observations over the Amazon basin. The seasonal and interannual variations in inundation have been evaluated against rain rate estimates from the Global Precipitation Climatology Project (GPCP) and water levels in wetlands, lakes, and rivers measured with satellite altimeters. The inundation data base is now being used for hydrology modeling and methane studies in GCMs.

Citation: Prigent, C., F. Papa, F. Aires, W. B. Rossow, and E. Matthews (2007), Global inundation dynamics inferred from multiple satellite observations, 1993–2000, *J. Geophys. Res.*, *112*, D12107, doi:10.1029/2006JD007847.

1. Introduction

[2]   Wetlands cover only ~5% of the Earth's ice-free land surface [e.g., *Matthews and Fung*, 1987; *Gosselink and Mitsch*, 2000] but exert major impacts on global biogeochemistry, hydrology, and wildlife diversity. First, they play a key role in global biogeochemical cycling of trace gases particularly methane (CH_4) and carbon dioxide (CO_2). They are the world's largest methane source and the only one dominated by climate. Approximately 20–40% of the world's total annual methane emission to the atmosphere comes from natural wetlands and irrigated rice fields [*Houweling et al.*, 1999; *Matthews*, 2000], and since preindustrial time, methane's contribution to radiative forcing is equal to roughly one half that of CO_2 [*Shindell et al.*, 2004]. Wetlands are also an important source and sink of carbon dioxide, with a net result that is ambiguous in some regions

[*Richey et al.*, 2002] but anticipated to respond to future changes in climate. Much progress has been made during the last 15 years on measuring and modeling CH_4-climate interactions in natural wetlands [e.g., *Walter et al.*, 2001a, 2001b; *Gedney et al.*, 2004], with considerable emphasis on boreal regions that are particularly vulnerable to climate-driven thawing of permafrost and consequent methane releases [*Christensen et al.*, 2003, 2004; *Walter et al.*, 2006]. However, a major obstacle to understanding the dynamics of current and future carbon exchanges has been the lack of observations of seasonal and interannual variations in inundation dynamics of wetlands and the rivers and lakes that influence them. Second, inundation associated with rivers, lakes, natural wetlands, and irrigation affects regional hydrological cycles. Water temporarily stored in flooded environments modulates temperature and heat fluxes and increases evaporation. In the boreal region, the role of flooded wetlands in cooling and humidifying the atmosphere exceeds that of lakes [*Krinner*, 2003]. *Coe* [2000] and *Krasnostein and Oldham* [2004] have developed models to predict the time varying flow and storage of water in hydrological systems. Finally, the biological diversity of inundated wetlands provides resources upon which numerous species of plants and animals depend for survival.

[3]   Defining wetlands and/or inundation is not straightforward; definitions vary according to research foci and, consequently, no overall consensus on the subject exists [e.g., *Reichhardt*, 1995]. Inundation occurs as a result of

[1] Laboratoire d'Etudes du Rayonnement et de la Matière en Astrophysique, Observatoire de Paris, Centre National de la Recherche Scientifique, Paris, France.
[2] Columbia University, NASA Goddard Institute for Space Studies, New York, USA.
[3] Laboratoire de Météorologie Dynamique, Institut Pierre-Simon Laplace, Centre National de la Recherche Scientifique, Université de Paris VI/Jussieu, Paris, France.
[4] NASA Goddard Institute for Space Studies, New York, USA.

flooding associated with rivers and lakes, rises in water table, snowmelt above permafrost, and irrigation. Some wetlands, especially in boreal regions underlain by permafrost, may be characterized by poorly drained, saturated soils that rarely or never experience inundated conditions. As a result, rigorous distinctions among wetlands, rivers and lakes may not be possible in some regions and/or seasons. Identifying and characterizing wetlands globally is further complicated by their distribution throughout tropical to boreal environments encompassing a wide variety of vegetation cover, hydrological regime, natural seasonality, and land-use impacts. Existing global or regional surveys represent various components of wetland and open water distributions comprising inundated and noninundated wetlands, lakes, rivers, and irrigated rice [*Matthews and Fung*, 1987; *Matthews et al.*, 1991; *Cogley*, 2003; *Loveland et al.*, 2000]. These static data sets reflect what is considered to be climatological maximum extent of active wetlands and inundation but lack information on temporal and spatial dynamics at seasonal or interannual timescales, while other studies of wetlands and/or inundation comprise local investigations. Some national inventories exist but are usually carried out for resource management or conservation purposes and consequently identify only those wetlands of particular interest to the purpose, e.g., wildfowl habitat. For instance, the convention on wetlands signed in Ramsar (Iran) in 1971 [*Ramsar Convention*, 1971] is a framework for national and international action for the preservation and wise use of wetlands. The convention identifies 1610 sites covering 1.45×10^6 km^2, which is ~30% of the natural wetland surface often adopted (5.30×10^6 km^2). Thus surveys underestimate inundated and nonundated wetlands of importance in global biogeochemical and hydrological studies.

[4] Remote sensing techniques employing visible, infrared, and microwave observations offer varying degrees of success in providing quantitative estimates of wetlands and inundation extent and monitoring natural and anthropogenic variations in these environments. *Sahagian and Melack* [1996] review the various techniques over a range of spatial resolutions that have been applied to wetlands. Low spatial resolution (e.g., 30 km) limits detection to large wetlands or to regions where the cumulative area of small wetlands comprises a significant portion of the field of view but has the advantage of frequent, often daily, coverage. High spatial resolution (e.g., 100 m), while providing more environmental information, suffers from poor temporal resolution, often limiting observations over large regions to just high/low water or warm/cold seasons. Optical and infrared remote sensing provide good spatial resolution but are limited by their inability to penetrate clouds and dense vegetation cover, especially in tropical wet seasons; they have proven useful in herbaceous environments such as the Okavango delta [*McCarthy et al.*, 2005]. Scatterometers and Synthetic Aperture Radar (SAR) are active microwave instruments that measure the backscattering coefficient of observed surfaces. When observed off-nadir, open-water surfaces are generally characterized by low backscattering coefficients and can be accurately delineated. When vegetation is present, nonspecular returns (multiple scattering) contaminate the signal, enhancing the backscattering coefficient and making the wetland detection site-specific.

Operating at low frequencies, these instruments can penetrate clouds and, to a certain extent, vegetation. SARs benefit from high spatial resolutions (10–50 m), whereas scatterometers have a typical spatial resolution of 25–50 km. SAR measurements have been used to map inundation from local to regional scales in both tropical [e.g., *Hess et al.*, 1990, 2003] and arctic environments [*Morrissey et al.*, 1996]. Satellite altimeters are radars that observe at nadir to measure surface topography and were originally designed for ocean applications. Techniques have been optimized to obtain accurate measurements (better than 10 cm) of water height in rivers, lakes, and wetlands from these satellite-borne instruments [e.g., *Birkett*, 1998; *Fung and Cazenave*, 2001]. Because altimeters have very narrow surface tracks, they do not provide sufficient spatial coverage to analyze the horizontal structure of water bodies except over boreal regions where their polar orbits offer better spatial coverage. Recently, *Papa et al.* [2006a] estimated the extent and seasonality of boreal inundation using observations from the Topex-Poseidon dual-frequency satellite radar altimeter.

[5] Passive microwave observations have long been shown to be valuable for delineating flooded areas [*Giddings and Choudhury*, 1989; *Choudhury*, 1991; *Sippel et al.*, 1998; *Mialon et al.*, 2005]. Flooding decreases emissivity in both linear polarizations and increases the polarization difference, especially at lower frequencies, due to differences in dielectric properties of water and soil or vegetation. The passive microwave signal can be contaminated by atmosphere, clouds, and rain, especially during maximum inundation extent that usually coincides with the periods of maximum rainfall. The signal is also altered by absorption and scattering by vegetation and modulated by surface temperature. Last, because of relatively coarse spatial resolution of microwave measurements available in the past (field of view of the order of 25–50 km across), regions with mixtures of open water and other complex surfaces produce ambiguous, intermediate-strength signals. Consequently, there is no absolute microwave-only indicator of open water for such mixed scenes. Therefore increasing the sensitivity of open water detection requires efforts to reduce the ambiguity introduced by these confounding factors. Most passive microwave studies are based solely on simple analyses of observations for limited areas, such as part of the Amazon basin in the work of *Sippel et al.* [1998] or boreal regions in the work of *Mialon et al.* [2005]. In these analyses the variable effects of vegetation, atmosphere (water vapor, clouds, and precipitation), and surface temperature are simply treated as scatter about a simple empirical relationship. Thus unquantified effects of systematic seasonal and interannual variations in these factors can distort time series estimates of inundation dynamics. An initial step to address the critical lack of observations of seasonal and interannual variations of inundation extent in wetlands and the rivers and lakes that influence them was the development of a globally applicable remote-sensing technique employing a suite of complementary satellite observations; monthly results of spatial and temporal dynamics of inundation were analyzed for one year [*Prigent et al.*, 2001a]. This method has recently been investigated over India for multiple years [*Papa et al.*, 2006b].
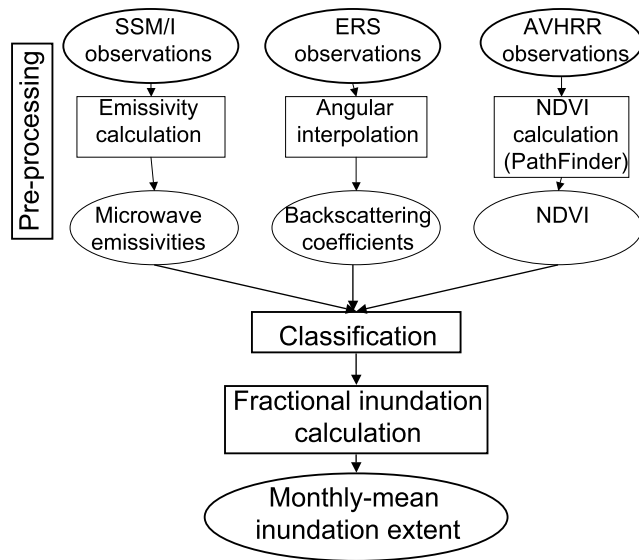
Figure 1. Schematic representation of the multisatellite method to estimate wetland extent.

[6] The objective of the present study is to present initial evaluation of the new, global multiyear data set and demonstrate the potential of this multisatellite method to derive spatial and temporal variations in global inundation extent and dynamics over decadal periods. In section 2 the satellite data sets and the methodology are summarized. Section 3 presents the global, monthly results for 1993–2000 and compares them with independent estimates at global and regional scales. In section 4 the seasonal and interannual dynamics of inundation extent is evaluated by comparison with precipitation and water heights in rivers, lakes, and wetlands as measured by satellite altimetry. Section 5 concludes this study and discusses new perspectives.

2. Summary of the Multisatellite Methodology

[7] This study employs the multisatellite method previously developed to detect inundated wetlands and to quantify their spatial and temporal dynamics which is described in detail by *Prigent et al.* [2001a] and summarized here. The method uses the following satellite observations covering a large portion of the electromagnetic spectrum: (1) Advanced Very High Resolution Radiometer (AVHRR) visible (0.58–0.68 μm) and near-infrared (0.73–1.1 μm) reflectances and the derived Normalized Difference Vegetation Index (NDVI); (2) passive microwave Special Sensor Microwave/Imager (SSM/I) measurements between 19 and 85 GHz (i.e., 1.58 cm to 0.35 cm in wavelength); and (3) active microwave backscattering coefficients at 5.25 GHz (wavelength =5.71 cm) from the scatterometer on board the European Remote Sensing (ERS) satellite. The satellite data sets are presented by *Prigent et al.* [2001b]. All the satellite observations are mapped to an equal area grid of 0.25° × 0.25° resolution at the equator (773 km^2), chosen to be both appropriate for global climate studies and compatible with spatial resolutions of the satellites. Monthly mean or monthly composite values are calculated from daily values from each satellite. Detection of inundation primarily relies on the passive microwave land-surface signal from SSM/I.

Relative to nonflooded lands, inundated regions are characterized by low microwave emissivities and high emissivity-polarization difference, even under dense canopy. To avoid interference from the atmospheric contribution and modulation by the surface temperature, the microwave emissivities are first calculated from the measured brightness temperatures. Over vegetated areas, the vegetation contribution is estimated with information from coincident ERS active microwave and NDVI observations. Because the ERS scatterometer shows minimal response to inundation but is very sensitive to high vegetation density [*Prigent et al.*, 2001b], it is used to assess vegetation contributions to the SSM/I passive microwave observations. In semiarid regions where bare surfaces and inundation can produce similar SSM/I signatures, NDVI information, rather than ERS observations, is used to resolve ambiguities.

[8] The method is a three step process (Figure 1). First, each satellite data set is preprocessed. The microwave emissivities of land surfaces are estimated from SSM/I passive microwave observations by removing the contribution from the atmosphere (including clouds and rain) and the modulation by the surface temperature, using ancillary data from visible and infrared satellite observations from the International Satellite Cloud Climatology Project (ISCCP) [*Rossow and Schiffer*, 1999] and the National Centers for Environmental Prediction (NCEP) reanalyses [*Kalnay et al.*, 1996]. The emissivity calculation is detailed by *Prigent et al.* [1997, 2006]. Because ERS observations are taken at different incidence angles and the repeat cycle is not short enough to provide multiple observations of the same scene with a single incidence angle during a month, a normalization approach is applied for all incidence angles between 25° and 50° for a month and the interpolated value at 45° is kept. The NDVI AVHRR products at 8 km generated under the joint NASA and NOAA Earth Observing System Pathfinder project [*James and Kalluri*, 1994] are projected and averaged over our equal area grid. Second, an unsupervised clustering algorithm using Kohonen topological maps [*Kohonen*, 1984] is used to merge the three sets of satellite observations. Kohonen topological feature maps are also called self-organizing topological maps: The distinguishing feature of this algorithm is the neighborhood requirement imposed on the prototypes so that when the algorithm has converged, prototypes corresponding to nearby points on the map grid have nearby locations in the data space. This approach has already shown potential to characterize large-scale patterns in the density and seasonality of the vegetation [*Prigent et al.*, 2001b] and was subsequently optimized for inundation detection. Examination of the maps resulting from the multisatellite clustering procedure carried out for each month enabled the selection of classes characterized by inundation. The last step, quantifying the fractional inundation of all pixels identified as inundated in the preceding step, employs a mixture model that relies on the statistical relationship between polarization differences and backscatter. Emissivity polarization differences increase with inundation fraction and decline with vegetation density, while the ERS scatterometer backscatter increases with vegetation density. We assume that for each vegetation density, polarization difference varies linearly with subpixel inundation fraction. Specifically, monthly flooded areas are

calculated by estimating subpixel coverage of inundation using the SSM/I passive microwave polarization difference at 37 GHz and applying a linear mixture model with end-members calibrated with the ERS observations to quantify the contribution of vegetation [see *Prigent et al.*, 2001a]. Global monthly mean maps of the inundation extent are created with a $0.25° \times 0.25°$ spatial resolution at the equator. The technique is globally applicable without any tuning for individual environments.

3. Results and Comparisons With Other Data

3.1. Global Results and Comparisons With Static Estimates

[9] Monthly multisatellite inundation estimates have been produced at a global scale for 1993–2000. Note that lacking additional external information, the technique captures, but does not discriminate among, inundated wetlands, rivers, small lakes, irrigated agriculture, or even ocean-contaminated coastal pixels. (For each given 773 km^2 pixel on the globe, all satellite observations falling within this box are considered: this does not necessarily restrict the full satellite field of view to fall within the pixel so a significant part of the radiation received by the satellite might actually come from neighboring pixels. In the results presented here, coastal pixels have been partly filtered as well as large inland water bodies. For each pixel in our grid, the fractional coverage of ocean and permanent inland water bodies is calculated from the International Geosphere-Biosphere Programme (IGBP) 1-min land ecosystem classification map [*Loveland et al.*, 2000]. Coastal pixels are defined as pixels that have at least one neighboring pixel that is covered by water at 70% or more (note that with this definition, coastal pixels represent 3.4% of the globe, i.e., their impact can be very significant if confused with inundated areas).) Figure 2 shows the annual maximum fractional inundation averaged over the 8 years regardless of month of maximum (Figure 2a), the variability of this annual maximum fractional inundation (standard deviation of the annual maximum) (Figure 2b), the mean number of inundated months (Figure 2c), and the most probable month of maximum inundation (Figure 2d). The maximum global inundation, which occurs in August, averages $5.86 \times 10^6 \text{ km}^2$ over the time series. The minimum inundated area occurs in December, averaging $2.12 \times 10^6 \text{ km}^2$ (i.e., 36% of the maximum).

[10] Our results are compared with independent data sets, each representing subsets of the inundation extent from the new data set. *Matthews and Fung*'s [1987] wetland fractions (Figure 3a) were derived from Operational Navigation Charts (ONCs) compiled for use by pilots; the spatial distribution, comprising both inundated and noninundated wetlands, likely reflects maximum extent but does not reflect seasonal dynamics. This $1° \times 1°$ resolution wetland data set was developed specifically to investigate the global distribution, environmental characteristics, and methane emissions of wetlands. Wetland-relevant subsets of three data sets (wetland vegetation, ponded soil, and inundation) with complementary strengths were merged to produce the final product. Thus while the spatial resolution is coarser than most satellite-derived land cover information, the thematic content is high. *Matthews et al.*'s [1991] monthly

cultivated-rice areas (Figure 3b) were derived by spatially distributing statistics of harvested-rice areas with seasonal cropping calendars for all rice-growing countries to produce a $1° \times 1°$ spatial resolution global data set. The 1 km resolution International Geosphere-Biosphere Programme (IGBP) DisCover data set [*Loveland et al.*, 2000] is the result of merging hundreds of vegetation classes into 17 more general land cover types "defined to meet the needs of IGBP core science projects." The distribution of inland water bodies for this data set was imposed using the hydrography layer of the Digital Chart of the World (DCW); the authors note that the DCW exaggerates the area of some water bodies such as the Aral Sea and Lake Chad. The fractional coverage of inland water bodies for each 773 km^2 grid point is calculated from the IGBP 1-min data set (Figure 3c).

[11] The new multisatellite inundation results exhibit very realistic distributions, with major inundated wetlands well delineated for all latitudes and environments. Inundation associated with major river systems is well captured, even in complex regions characterized by extensive flooding below dense vegetation canopies (e.g., the Amazon and Congo Rivers), with potentially high fractional inundation extent (Figure 2a), low variability in the annual maximum (Figure 2b), and quasi-permanent flooding (Figure 2b). In semiarid regions in southern Africa, the seasonal wetlands (e.g., the Okavango Delta in Botswana and the Etosha Pan in Namibia) are realistically captured. Irrigated rice exhibits a strong signature, especially in southeast Asia where rice dominates the agricultural landscape (Figure 2a and Figure 3a). Inundation duration (Figure 2c) and month of maximum inundation (Figure 2d) are consistent with the seasonality of rice-cropping [*Matthews et al.*, 1991]. For example, Chinese rice crops are growing earlier than those in the surrounding countries; the triple rice cropping is common in southern China and it translates into earlier and longer flooding period than elsewhere. In India where double-cropping of rice dominates, growing seasons over the country are more variable but are highest from July to October. Large inundated areas in northern Canada are consistent with the ubiquitous presence of small lakes (Figure 2a and Figure 3c). The inundated region around the Ob River in northern Russia is also well reproduced and has been assessed with independent data by *Papa et al.* [2006a]. In boreal regions, inundation periods (Figure 2c) decline from 5 months at 45°N to 3 months around 10° northward, consistent with the increasing length of snow cover and frozen conditions, with the most probable month of maximum inundation in these latitudes during spring melt. In tropical regions, maximum inundation, controlled primarily by precipitation, occurs during summer rains; note the consistent inversion in months of maximum inundation between the northern and southern hemispheres. In contrast, because inundation in midlatitudes of Europe and the US is controlled primarily by temperature and local snowmelt, soils in these regions experience maximum saturation and inundation mostly in late winter and spring.

[12] Comparisons of the IGBP fractional permanent water coverage (Figure 3c) with our wetland estimates shows that the multisatellite retrieval produces fewer inundated locations in some regions (central Russia and western Canada) than are present in the IGBP data. Given the large footprint of the satellite radiometers, small water fractions can
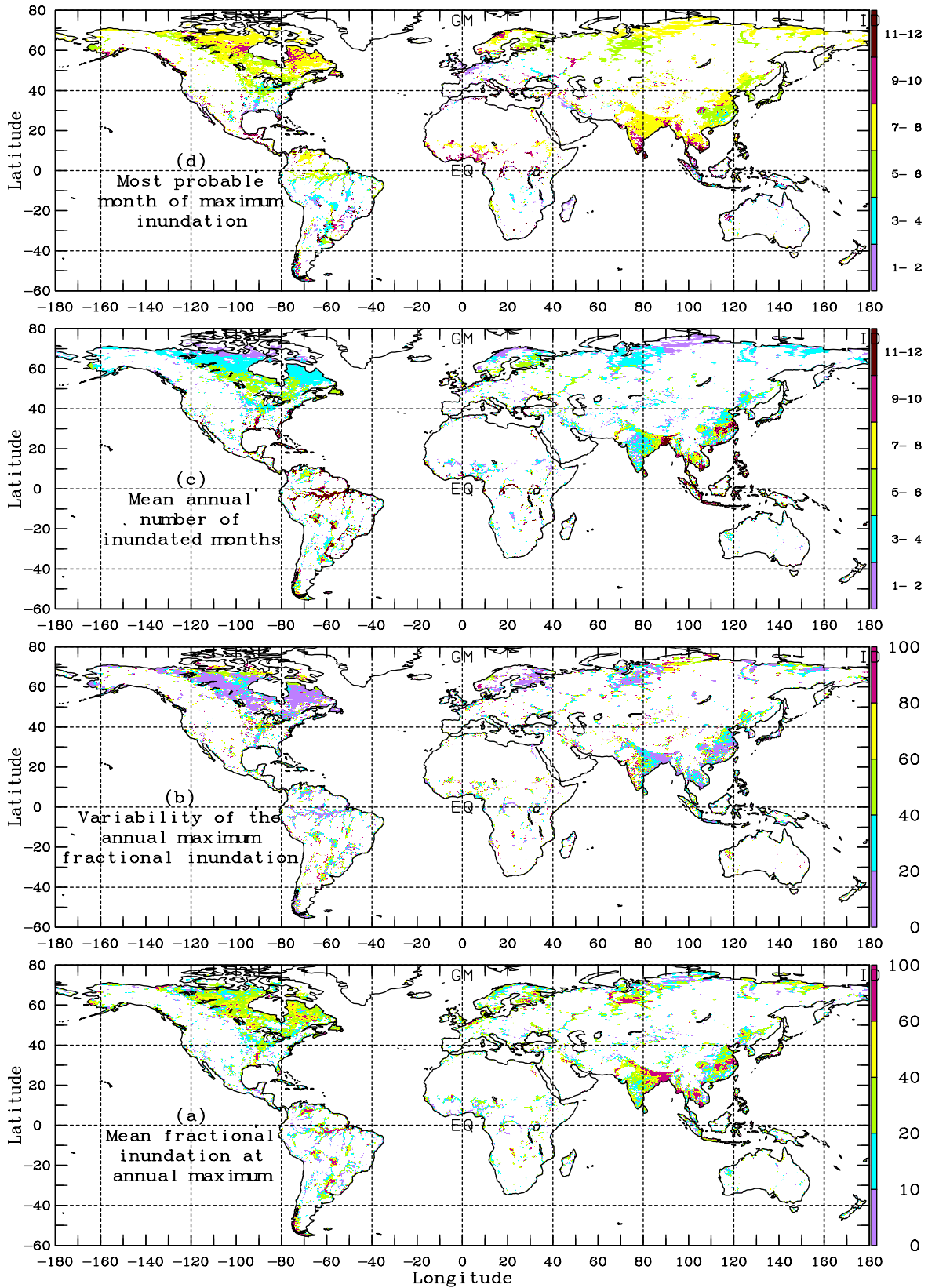
Figure 2. Global satellite-derived inundation results over the 1993–2000 period with a 773 km^2 spatial resolution (i.e., equal area grid of 0.25° × 0.25° at the equator). From bottom to top: (a) the annual maximum fractional inundation averaged over the 8 years, (b) the variability of the annual maximum fractional inundation (standard deviation of the maximum over the 8 years), (c) the mean annual number of inundated months, and (d) the most probable month of maximum inundation.
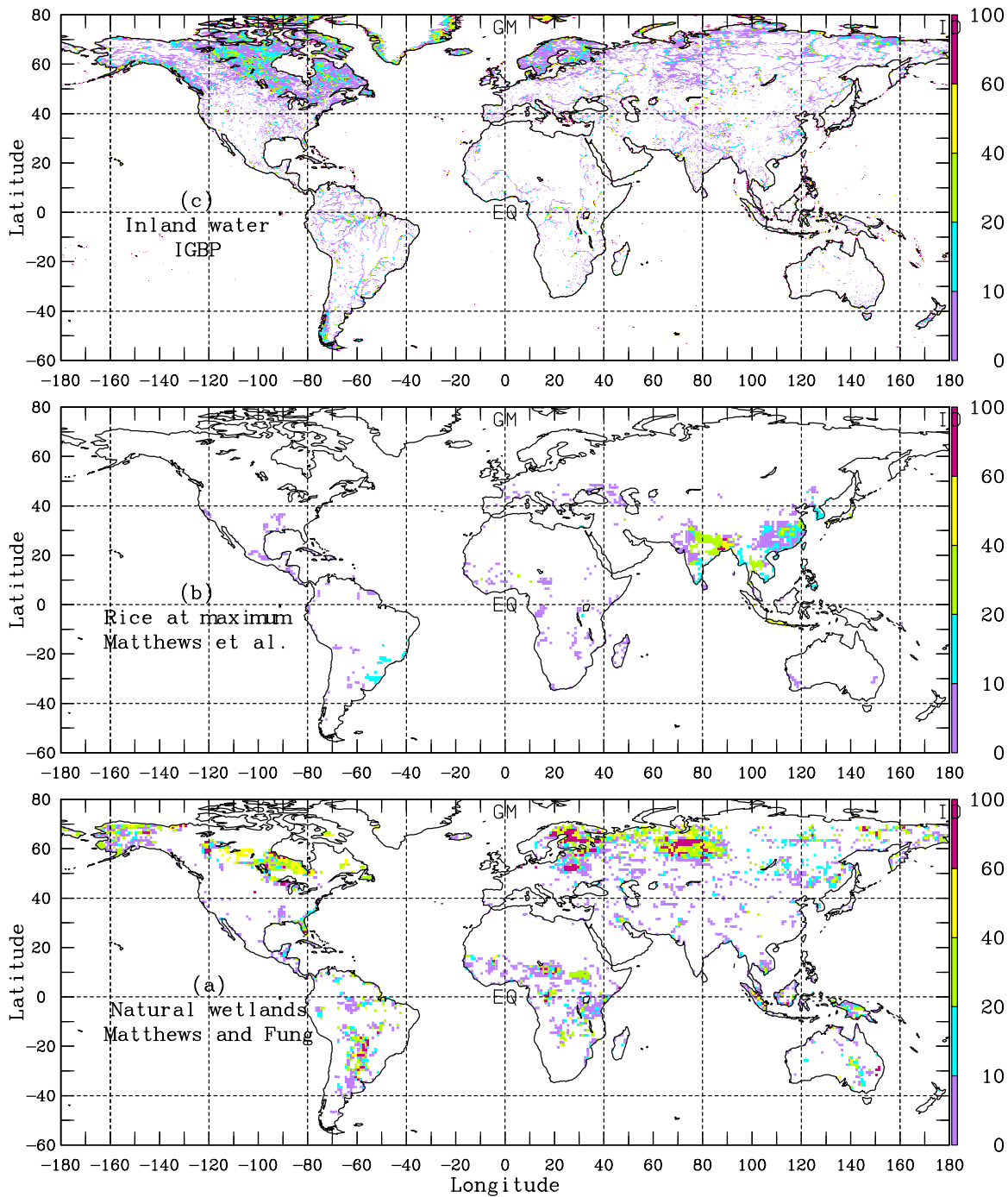
Figure 3. From bottom to top: (a) the natural wetland fraction from *Matthews and Fung* [1987] on a 1° × 1° grid, (b) the fractional extend of rice paddies at maximum from *Matthews et al.* [1991] on a 1° × 1° grid, and (c) the fraction of inland permanent water from IGBP for each 773 km² grid cell.

represent only a very small fraction of the field of view: The radiometer and the retrieval algorithm might not be sensitive enough to detect these small water fractions. However, while the new technique is expected to underestimate small, isolated water bodies, it is difficult to determine the extent of this effect. For the 50°N60°N to 30°E100°E region, histograms of maximum fractional inundation from the multisatellite method and from the IGBP inland permanent water (Figure 4) confirm that the latter contains a very large number of pixels with less than 10% water coverage and

very few larger water features. If the IGBP data are accurate, it appears that the multisatellite approach misses most inland water bodies that cover less than 10% of the pixels in this region. This can be seen as a measure of the sensitivity of our multisatellite detection method: it is expected that this sensitivity varies with the environment, the higher the vegetation density the lower the sensitivity, the 10% corresponding to rather densely forested region.

[13] The seasonal and interannual variations of inundated areas are presented on Figure 5, globally and by latitude
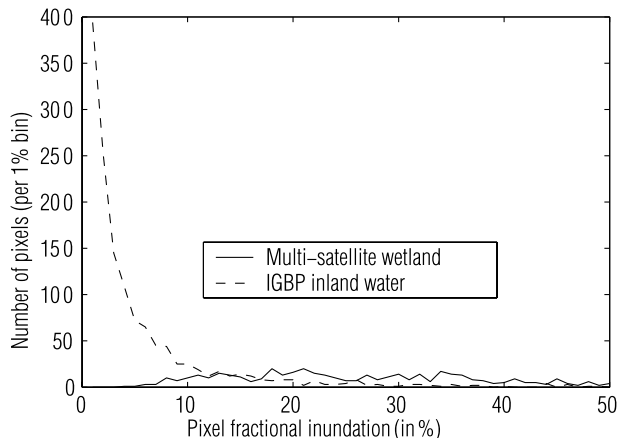
Figure 4. For the 50°N60°N to 30°E100°E region, histograms of the fractional inundation estimate at maximum from the multisatellite method (solid line) and inland water fraction from IGBP (dashed line) for the same 773 km^2 grid.

zones. The static estimates for all wetlands [*Matthews and Fung*, 1987; *Cogley*, 2003], as well as seasonal rice areas [*Matthews et al.*, 1991] are also indicated. The wetland estimate from *Cogley* [2003] includes irrigated rice for some regions (China) but not others (India). Contrary to the IGBP data set, the Cogley data distinguishes inland water bodies from the ocean fractions, making it easier to subtract the coastal contribution. However, similar to IGBP, both the wetland and lake distributions of Cogley [see *Prigent et al.*, 2001, Figures 3e–3f] may overrepresent small features. Globally, our estimate of inundated are at maximum (5.86 × 10^6 km^2 averaged for 1993–2003) is in reasonable agreement with several global inventories representing similar but not identical features identified in the new data. Matthews' wetlands (5.20 × 10^6 km^2) and irrigated rice (1.05 × 10^6 km^2) total 6.25 × 10^6 km^2, while Cogley's total for wetlands and perennial lakes is 5.70 × 10^6 km^2. We note, however, that the two latter wetland areas include noninundated wetlands not captured in the new data set and that Cogley may overestimate small lakes. Over tropical and subtropical Asia, our new estimate shows a seasonal cycle consistent with well-documented rice agriculture [*Matthews et al.*, 1991]. At midlatitudes and over the tropics, a rather strong interannual variability is observed, both in the minimum and maximum extents of the inundation. These patterns have been checked, with particular attention paid to the peaks in maximum extent over the tropics in 1994 and 1998 and the significant decrease in wetland extent from 1998 to 2001 at midlatitude and over the tropics. Evaluation of the data set with independent estimates of other surface parameters (precipitation and river water level) tends to confirm the accuracy of these observations. In addition, these interannual patterns also agree well with observed atmospheric methane anomalies [*Dlugokencky et al.*, 2001; *Bousquet et al.*, 2006].

3.2. Direct Comparison With SAR Estimates Over the Amazon Basin

[14] Long-term and higher spatial resolution surveys of wetland extent over large regions are very scarce. SAR

imagery can provide estimates with much better spatial resolution than our product but suffers from a lack of temporal coverage. One study of flooding in the Amazon basin for both low-water (September–October 1995) and high-water (May–June 1996) conditions is that of *Hess et al.* [2003] based on 100-m resolution L-band SAR observations from the Japanese Earth Resources Satellite-1 (JERS-1). Figure 6 compares our estimates (Figure 6, bottom) with the Hess et al. results (Figure 6, top) for the same time periods. The SAR estimates are projected onto the 0.25° × 0.25° equal area grid (773 km^2) for comparison purposes. The spatial structures of the inundation are very similar. The total SAR-derived flooded area is 118,000 km^2 (243,000 km^2) for this 18° × 8° region as compared to our results of 105,000 km^2 (171,000 km^2) for low (high) water stage. The difference in total flooded area is larger during high water stage. With its much better spatial resolution, the SAR can more accurately estimate small areas that are flooded in generally dry conditions or small dry areas in generally flooded conditions, whereas our lower resolution observations may miss such small fractional coverages. Figure 7 compares the histograms of the fractional inundation extent (on the 0.25° × 0.25° equal area grid) from the two analyses and confirms this expectation in part. During low water stage, more pixels with low fractional inundation are detected by the SAR relative to our product, but also there is a tendency for our analysis to overestimate the
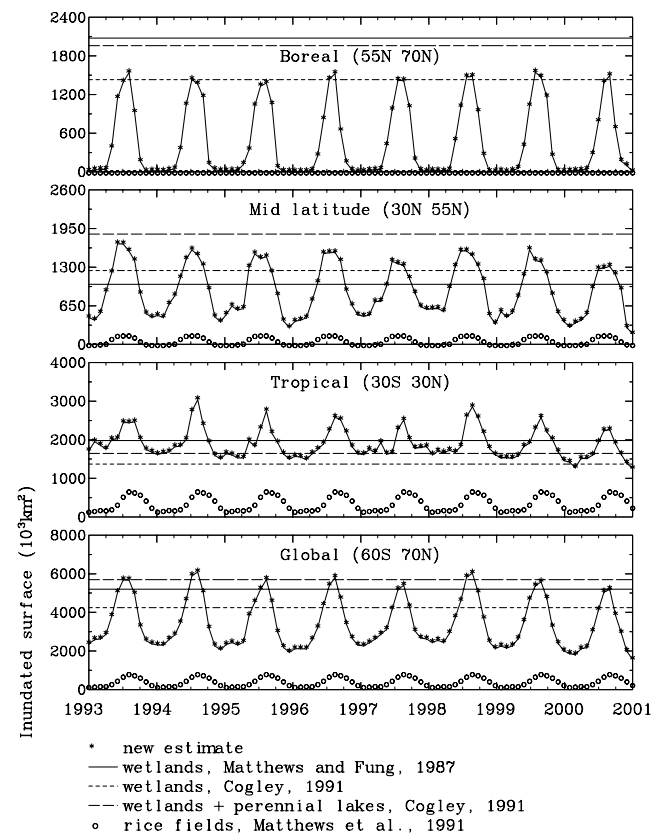

Figure 5. Seasonal variations of the inundated areas globally and by latitude zones over the 1993–2000 period. Estimates from *Matthews et al.* [1987, 1991] and *Cogley* [2003] are also indicated.
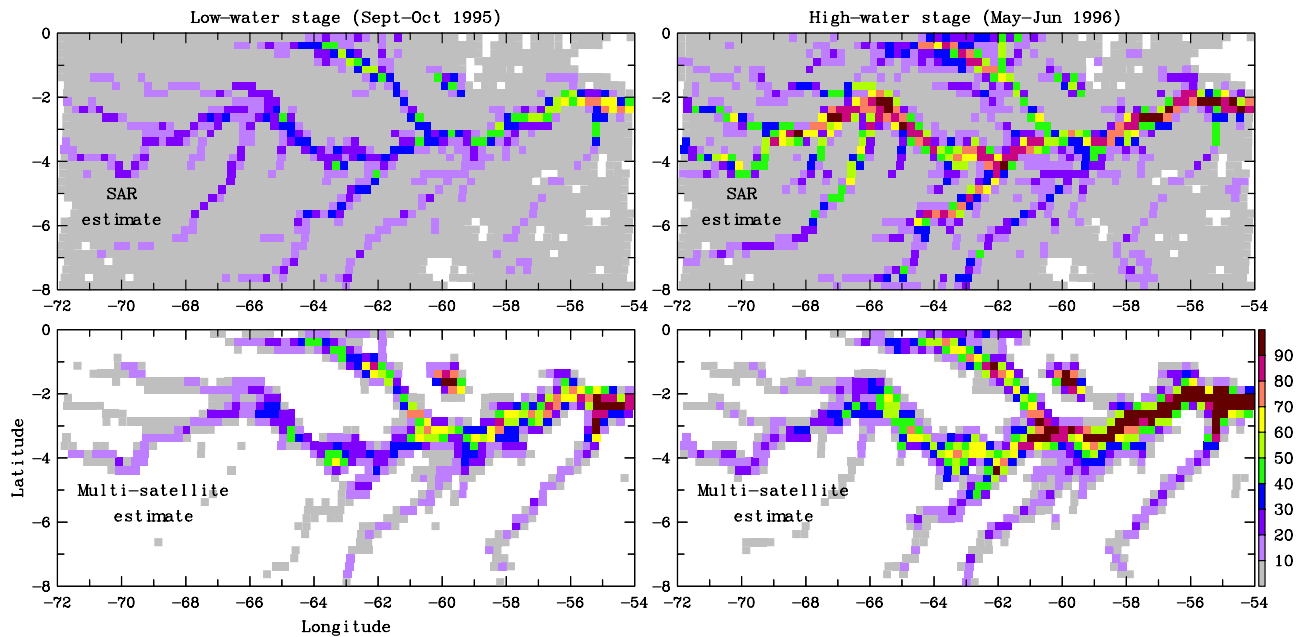
Figure 6. Comparison of (top) the multisatellite inundation estimates with (bottom) the SAR estimates from *Hess et al.* [2003] for the same periods of time, in terms of fractional inundation over the equal area pixels of 773 km^2, showing (left) the low-water stage during September–October 1995 and (right) the high-water stage during May–June 1996.

higher fractional inundations as well. However, both of these biases are smaller during high water stage. This result may be explained by more frequent areas with small fractional inundation during low water stage, as expected, but also by the more frequent occurrence of small dry patches in areas with large fractional inundation. This situation is similar to that encountered in the determination of cloud cover fraction by satellites: lower-resolution products, when estimating areas by counting pixels and using the same detection threshold, tend to overestimate cloud fractions relative to higher-resolution products both because they overestimate the area covered by very small clouds and because they miss holes in clouds [*Wielicki and Parker*, 1992; *Rossow and Garder* 1993]. However, a very strict detection threshold produces a systematic overestimate, whereas a less strict threshold allows for both overestimates and underestimates, producing a small average error. Likewise, our lower-resolution product can yield a less biased estimate using a finite detection threshold as we did. However, we note that the SAR product still has some artifacts that have not been removed (radar speckle, lagged gain changes) and that the boundary between flooded and not flooded signals is still somewhat ambiguous [*Hess et al.*, 2003], as in our analysis, so there is uncertainty in the detection threshold for SAR as well.

4. Evaluation of the Wetland Estimates Through Their Relationship With Other Variables

[15] Given the scarcity of global, multiyear inundation estimates, the seasonal and interannual variabilities of the multisatellite inundation results are evaluated by comparison with related hydrological variables that are measured on a more regular basis.

4.1. Relation to Precipitation

[16] The inundation characteristics depend on the distribution and intensity of precipitation as well as on the land surface properties that control how precipitation is partitioned among evaporation, storage at the surface and at depth, and runoff. Flooding can occur in response to locally intense precipitation as well as snow melt or heavy precipitation in upstream locations. In that case, inundation and precipitation are separated in both time and space. Keeping
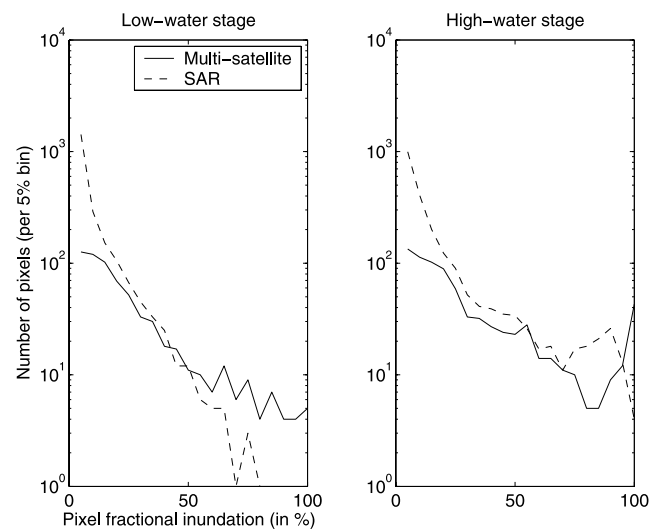

Figure 7. Histograms of the inundation estimates from the multisatellite method (solid line) and the SAR method *Hess et al.* [2003] (dashed line) for (left) the low-water stage during September–October 1995 and (right) the high-water stage during May–June 1996.
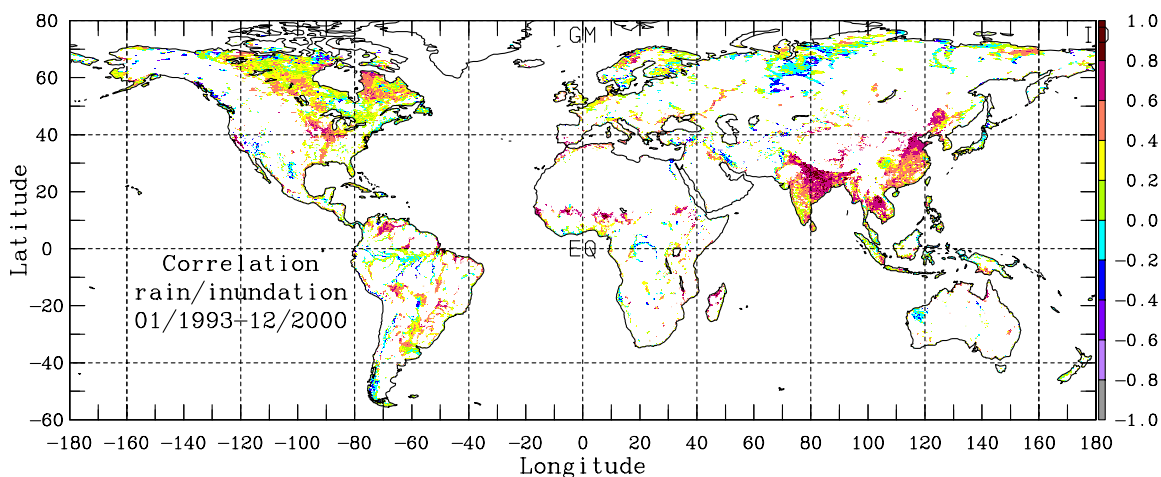
Figure 8. Temporal correlation between the multi-satellite inundation estimates and the GPCP surface precipitation for the 1993–2000 period (months with snow are excluded from the calculation).

this in mind, we examine the relationship between the satellite-derived inundated surfaces and precipitation, the monthly mean Global Precipitation Climatology Products (GPCP) are used. GPCP quantifies the distribution of precipitation around the globe over many years from merged infrared and microwave satellite data and rain gauge measurements [*Adler et al.*, 2003]. (Over land, the microwave-derived rain rate, when used, is related to the scattering by large cloud particles at 85 GHz: these channels are not used in our inundation estimates.) For each location, we calculate the linear correlation between the monthly mean inundated surfaces and precipitation estimates from January 1993 to December 2000. The results are mapped in Figure 8. The linear correlation is positive and large (above 0.6) in regions with strong precipitation seasonal cycles and rather low vegetation density. For instance, in India where a monsoon regime dominates the precipitation cycle, the inundation extent is strongly correlated with precipitation. Boreal wetlands are essentially due to snow melting and as a consequence, their extent is less correlated with the precipitation rate (e.g., the Ob region in Russia). In other regions, the precipitation and inundation cycles are lagged. Figure 9 shows the linear correlation between precipitation and inundation in South America (Figure 9a), as well as the time-lagged correlation at maximum absolute correlation (Figure 9b) and the corresponding time lag of the maximum correlation in months (only for regions where the absolute correlation is larger than 0.4; a positive time lag means precipitation happens before inundation) (Figure 9c). The linear correlation is generally higher in the surrounding part of the basin and decreases around the main stream (Figure 9a). This is especially clear around the Pantanal, with the correlation increasing with the distance from the Paraguay River. Around the main stem of the Amazon River, the correlation is also relatively low and increases along the tributaries. The time lag between precipitation and inundation cycles decreases with increasing distance from the main stream (Figure 9c). Further upstream, the local precipitation more directly governs the wetland extent.

[17] Figure 10 compares the time series of the inundation and precipitation in six different regions in South America

(both variables are normalized: the mean value is subtracted and the result is divided by the standard deviation over the 8 years). In most regions, the precipitation and inundation cycles show similar behavior, although precipitation often precedes the inundation. On the contrary, around the Parana, there is not a clear link between precipitation and inundation, the inundation being likely due to precipitation events upstream.

[18] El Nino/Southern Oscillation (ENSO) induces large changes in the precipitation patterns leading to drought and flood depending on the region [*Ropelewski and Halpert*, 1987, 1989]. The 1997–1998 El Nino and the 1998–1999 La Nina that quickly followed were accompanied by severe precipitation anomalies over the continents, especially around the tropics. *Curtis et al.* [2001] analyzed the GPCP precipitation patterns during the 1997–1999 ENSO and confirmed the quality of the GPCP products during such events. Figure 11 compares the monthly mean anomalies in the satellite-derived wetland extents to the monthly mean anomalies in the GPCP precipitation estimates over South America for four periods during the 1997–1999 ENSO. Both the spatial and temporal patterns agree well, with related alternating wet and dry anomalies in wetland extents and precipitation, in latitude and time. For instance, the Parana region (north of Buenos Aires) is drier than usual from March to September 1997, wetter from October 1997 to September 1998, and drier from October 1998 to March 1999. On the other hand, the Orinoco region in Venezuela is drier up to March 1998, wetter from April 1998 to September 1998, and close to normal later. These spatial and temporal patterns are consistent with the analysis by *Ropelewski and Halpert* [1987, 1989]. The satellite inundation estimates capture well the drought and floods related to the ENSO and can be used as tracers of the ENSO over land.

4.2. Comparison With Water Level Estimates From Satellite Altimeter Observations

[19] Inundation extent and water height are two related characteristics of the wetlands that combined together with topographic information could provide an estimate of the water storage in the flooded plain. The water levels in rivers
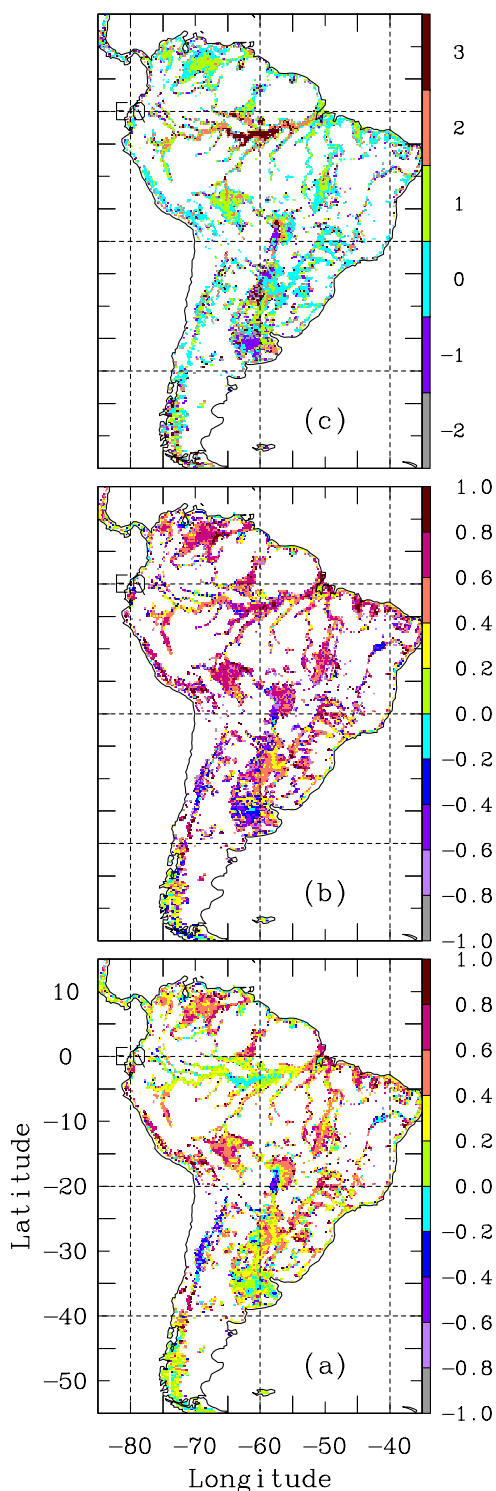
Figure 9. Over South America, from bottom to top, (a) temporal correlation between the multisatellite inundation estimates and the GPCP surface precipitation as Figure 8, (b) maximum temporal correlation between the multi-satellite inundation estimates and the GPCP surface precipitation when one is lagged in time with respect to the other (c) time lag in month to obtain the maximum correlation (positive time lag when the precipitation happens before the inondation).

and wetlands have been estimated from satellite altimetry [e.g., *Birkett*, 1998; *Fung and Cazenave*, 2001] with very good agreement with river gauge measurements. M.-C. Gennero et al. provide almost a decade of river and lake heights all over the world, derived from the Topex-Poseidon altimeter observations (available at http://www.legos.obs-mip.fr/soa/hydrologie/hydroweb/Page_2.html). The variations of the wetland extent for the 8 years are compared systematically with the water level altimeter estimates derived from the Topex-Poseidon altimeter observations for all the coincident locations available from http://www.legos.obs-mip.fr/soa/hydrologie/hydroweb/Page_2.html. Figure 12 displays the normalized 8-year time series for four locations representing a variety of environments, from
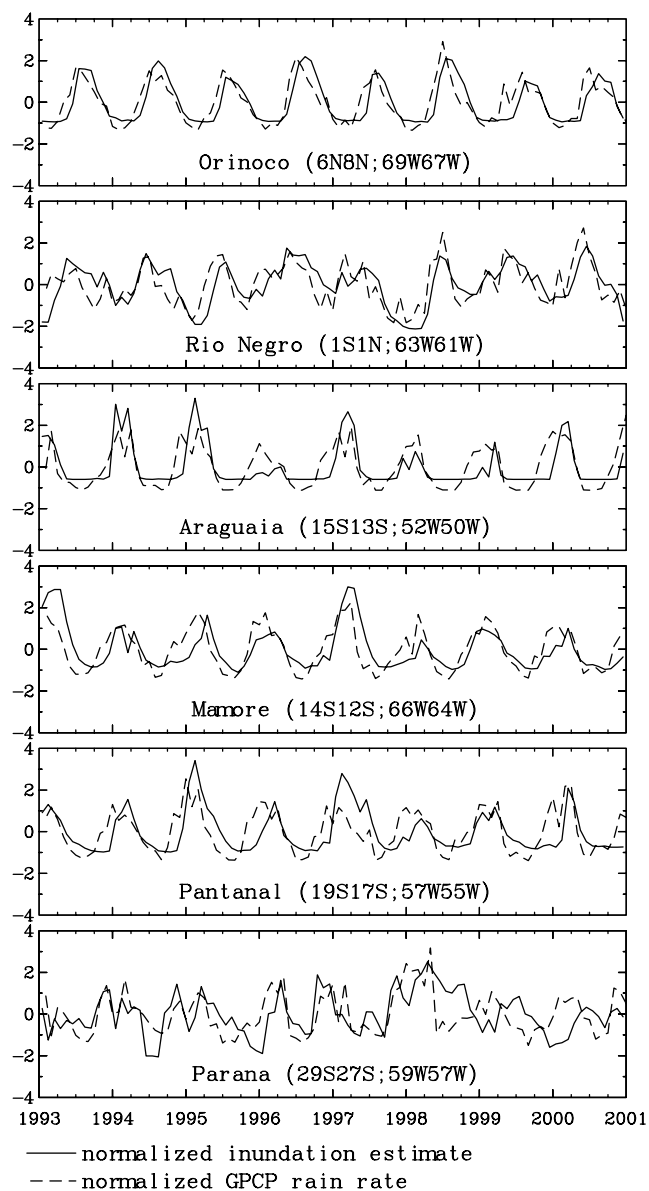

Figure 10. Examples of time series of satellite-derived inundation extent and GPCP precipitation in South America during the 1993–2000 period. Both variables are normalized (the mean is subtracted and the resulting values are divided by the standard deviation over the period).
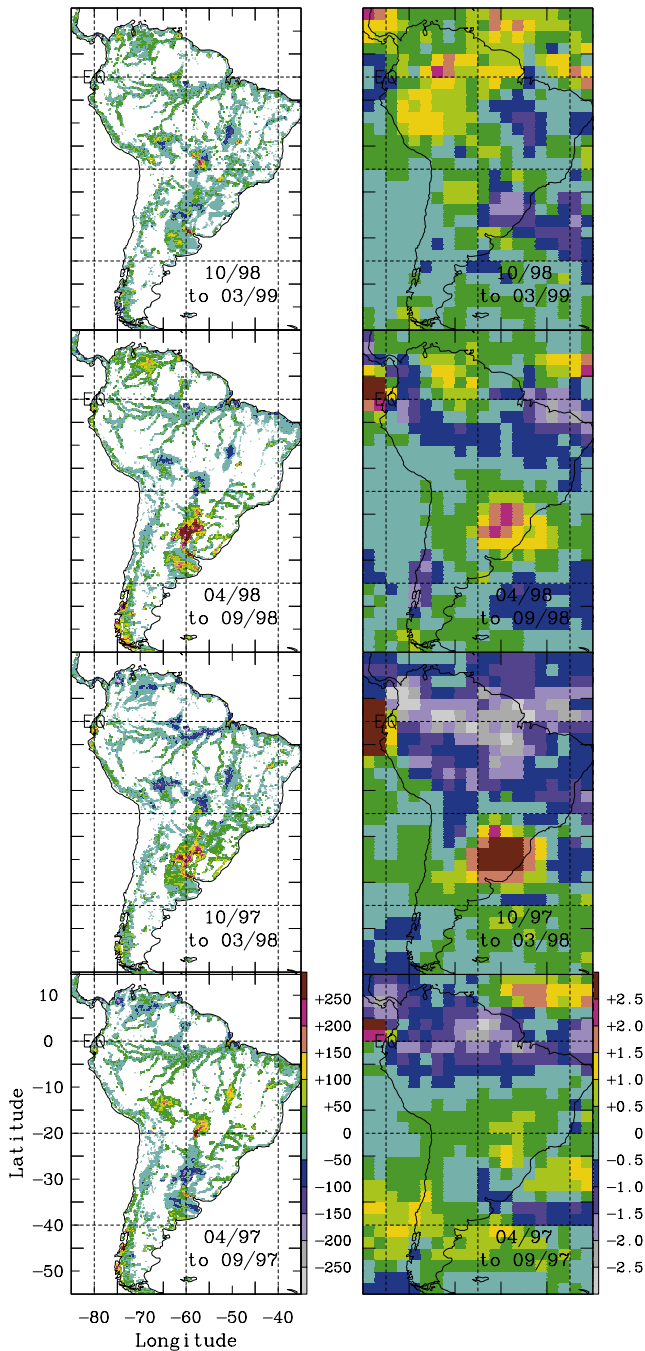
Figure 11. (left) The monthly mean anomaly of the satellite-derived inundation extent (in km^2 per pixel of 773 km^2) for four periods of time during the 1997–1999 Nino-Nina Southern Oscillation and (right) the same for the GPCP precipitation in mm/day.

independent methodologies.) Regardless of the environment, the seasonal and interannual patterns of the two time series agree exceptionally well, even for cases with a complex variability (e.g., the Pantanal region). For the Niger cases, two exceptional maxima in 1994 and 1999 clearly exceed the normal years in the wetland extent series but are not reproduced by the altimeter water level. The GPCP precipitation has been checked: the 1994 and 1999 rain rates were above average. Differences between dynamics in water levels and inundated area might be explained in terms of the very flat basin topography: with no topographical obstacles to impede expansion, flood waters can spread to cover large areas without a correlated increase in water level.

5. Conclusions and Perspectives

[20] This study presents the first global estimate of wetland extent and dynamics over almost a decade, with monthly mean values of the inundated fractional extent for each 0.25° × 0.25° over the globe for the 1993–2000 period. Inundated surfaces, comprising both natural wetlands and irrigated fields, are estimated using a clustering
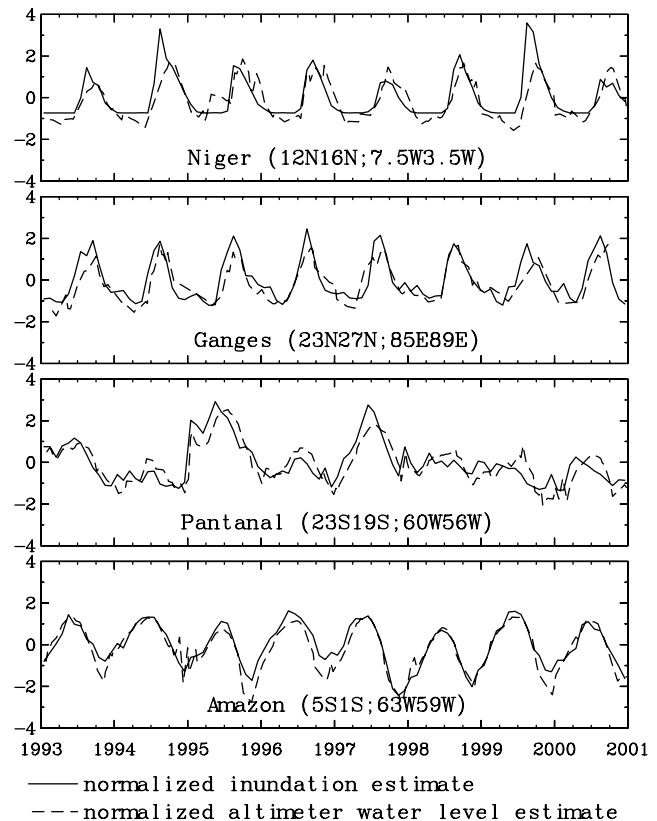

Figure 12. Comparison of the time series of the satellite-derived inundation extent and the Topex-Poseidon altimeter water level for four locations during the 1993–2000 period. The inundation extent is calculated over a 4° × 4° area centered on the altimeter water level estimate. Both variables are normalized (the mean is subtracted and the resulting values are divided by the standard deviation over the period).

tropical forest to semiarid regions. The wetland extent estimates are averaged over a 4° × 4° region around the altimeter measurement locations. The figure clearly shows strong agreement between the two data sets for the seasonal cycle over the 8 years. (The altimeter water level estimate and the multisatellite wetland product are completely independent, being estimated from different satellites and using

analysis of a suite of satellite observations including passive and active microwaves, visible, and near-IR observations, together with a linear mixing model to estimate flooded pixel fractions. Combining observations from different instruments makes it possible to capitalize on their complementary strengths, to extract maximum information about inundation characteristics, and to minimize problems related to one instrument only. The technique is globally applicable without any tuning for particular environments. Global inundated area varies from a 5.86×10^6 km^2 average maximum over the 1993–2000 period to a 2.12×10^6 km^2 minimum, consistent with previous independent static estimates from *Matthews et al.* [1991] or *Cogley* [2003]. The multisatellite wetland estimates also show good agreement with regional high-resolution SAR inventories. The seasonal and interannual variations of inundation have been evaluated with respect to rain rate estimates (GPCP) and altimeter river height levels. Not only are the seasonal patterns well captured regardless of the environment but also the interannual variability is consistent with the other related hydrological variables.

[21] Lacking comprehensive detailed assessment of the performance of the multisatellite detection method against independent data, as well as concerns about the realism of independent data, it is not possible provide a rigorous error estimate. However, the technique probably underestimates small wetlands comprising less than 10% fractional coverage of equal-area grid cells (i.e., ~80 km^2 in ~800 km^2 pixels) compared to SAR estimates.

[22] The time series is currently limited to January 1993 through December 2000. In 2001 the ERS scatterometer began to encounter several problems that impact this study. Efforts are now underway to use the scatterometer SeaWinds from the QuikSCAT satellite instead: fine tuning of the methodology will be required to account for the differences in the instrument characteristics (higher spatial resolution and observations at 13.4 GHz).

[23] Accurate modeling of spatial and temporal dynamics of inundation, which includes lakes, rivers, and a substantial portion of the world's wetlands, has remained problematic due in part to the absence of data and techniques to quantifying these complex systems. This new multisatellite database is now being used to calibrate and evaluate land surface hydrology models such as the ISBA model from Météo-France [*Decharme*, 2005]. A promising synergy with radar altimetry can also provide crucial information about hydrological parameters such as water storage and river discharge and is now under investigation. Simple parameterizations of methane emission as a function of climate have been developed from complex process models for wetlands [*Walter et al.*, 2001a, 2001b] and introduced into climate models [*Shindell et al.*, 2004]. Realistic inundation dynamics derived from the satellite observations provide the opportunity to develop and calibrate simulations of methane emissions associated with surface hydrology; initial efforts are already underway [*Bousquet et al.*, 2006].

References

Adler, R. F., et al. (2003), The version 2 Global Precipitation Climatology Project (GPCP) monthly precipitation analysis (1979-present), *J. Hydrometeorol.*, *4*, 1147–1167.

Birkett, C. M. (1998), Contribution of the TOPEX NASA radar altimeter to the global monitoring of large rivers and wetlands, *Water Resour. Res.*, *34*, 1223–1239.

Bousquet, P., et al. (2006), The contribution of anthropogenic and natural sources to the variability of atmospheric methane, *Nature*, *443*, 439–443, doi:10.1038/nature05132.

Choudhury, B. J. (1991), Passive microwave remote sensing contribution to hydrological variables, *Surv. Geophys.*, *12*, 63–84.

Christensen, T. R., A. Ekberg, L. Strom, and M. Mastepanov (2003), Factors controlling large scale variations in methane emissions from wetlands, *Geophys. Res. Lett.*, *30*(7), 1414, doi:10.1029/2002GL016848.

Christensen, T. R., T. Johansson, H. J. Akerman, and M. Mastepanov (2004), Thawing sub-arctic permafrost: Effects on vegetation and methane emissions, *Geophys. Res. Lett.*, *31*, L04501, doi:10.1029/2003GL018680.

Coe, M. (2000), Modelling teerrestrial hydrologic systems at the continental scale: Testing the accuracy of an atmospheric GCM, *J. Clim.*, *13*, 686–704.

Cogley, J. (2003), GGHYDRO-Global Hydrographic Data, release 2.3, *Tech. Not. 2003-1*, Dept. of Geogr., Trent Univ., Peterborough, Ont., Canada.

Curtis, S., R. F. Adler, G. J. Huffman, E. Nelkin, and D. Bolvin (2001), Evolution of tropical and extratropical precipitation anomalies during the 1997 to 1999 ENSO cycle, *Int. J. Climatol.*, *21*, 961–971.

Decharme, B. (2005), Développement et validation d'une modélisation hydrologique globale incluant les effets sous-maille et la représentation des zones inondées, Ph.D. thesis, Toulouse Univ., France.

Dlugokencky, E. J., B. P. Waleter, K. A. Masarie, P. M. Lang, and E. S. Kasischke (2001), Measurements of an anomalous global methane increase during 1998, *Geophys. Res. Lett.*, *28*, 499–502.

Fung, L. L., and A. Cazenave (2001), *Satellite Altimetry and Earth Science: A Handbook of Techniques and Applications*, Elsevier, New York.

Gedney, N., P. M. Cox, and C. Huntingford (2004), Climate feedback from wetland methane emission, *Geophys. Res. Lett.*, *31*, L20503, doi:10.1029/2004GL020919.

Giddings, L., and B. J. Choudhury (1989), Observation of hydrological feature with Nimbus-7 37 GHz data applied to South America, *Int. J. Remote Sens.*, *10*, 1673–1686.

Gosselink, G. J., and J. W. Mitsch (2000), *Wetlands*, 3d ed., John Wiley, Columbus, Ohio.

Hess, L. L., J. M. Melack, and D. Simonett (1990), Radar detection of flooding beneath the forest canopy: A review, *Int. J. Remote Sens.*, *11*, 1313–1325.

Hess, L. L., J. M. Melack, E. M. L. M. Novob, C. C. F. Barbosac, and M. Gastil (2003), Dual-season mapping of wetland inundation and vegetation for the central Amazon basin, *Remote Sens. Environ.*, *87*, 404–428.

Houweling, S., T. Kaminski, F. Dentener, J. Lelieveld, and M. Heinmann (1999), Inverse modeling of methane sources and sinks using adjoint of a global transport model, *J. Geophys. Res.*, *104*, 26,137–26,160.

James, M. E., and S. N. V. Kalluri (1994), The Pathfinder AVHRR land data set: An improved coarse resolution data set for terrestrial monitoring, *Int. J. Remote Sens.*, *15*, 3347–3364.

Kalnay, E., et al. (1996), The NCEP/NCAR 40-year reanalysis project, *Bull. Am. Meteorol. Soc.*, *77*, 437–470.

Kohonen, T. (1984), *Self-Organization and Associative Memory*, Springer, New York.

Krasnostein, A. L., and C. E. Oldham (2004), Predicting wetland water storage, *Water Resour. Res.*, *40*, W10203, doi:10.1029/2003WR002899.

Krinner, G. (2003), Impact of lakes and wetlands on boreal climate, *J. Geophys. Res.*, *108*(D16), 4520, doi:10.1029/2002JD002597.

Loveland, T. R., B. C. Reed, J. F. Brown, D. O. Ohlen, J. Zhu, L. Yang, and J. W. Merchant (2000), Development of a global land cover characteristics database and IGBP DISCover from 1-km AVHRR data, *Int. J. Remote Sens.*, *21*, 1303–1330.

Matthews, E. (2000), Wetlands, in *Atmospheric Methane: Its Role in the Global Environment*, edited by M. A. K. Khalil, pp. 202–233, Springer, New York.

Matthews, E., and I. Fung (1987), Methane emission from natural wetlands: Global distribution, area, and environmental characteristics of sources, *Global Biogeochem. Cycles*, *1*, 61–86.

Matthews, E., I. Fung, and J. Lerner (1991), Methane emission from rice cultivation: Geographic and seasonal distribution of cultivated areas and emissions, *Glob. Biogeochem. Cycles*, *5*, 3–24.

McCarthy, J., T. Gumbricht, and T. S. McCarthy (2005), Ecoregion classification in the Okavango Delta, Botswana from multitemporal remote sensing, *Int. J. Remote Sens.*, *26*, 4339–4357.

Mialon, A., A. Royer, and M. Fily (2005), Wetland seasonal dynamics and interannual variability over northern high latitudes, derived from microwave satellite data, *J. Geophys. Res.*, *110*, D17102, doi:10.1029/2004JD005697.

Morrissey, L., S. Durden, G. Livingston, J. Stearn, and L. Guild (1996), Differentiating methane source areas in Arctic environments with multispectral ERS-1 SAR data, *IEEE Trans. Geosci. Remote Sens.*, *34*, 667–673.

Papa, F., C. Prigent, B. Legresy, and F. Rémy (2006a), Inundated wetland dynamics from remote sensing: using Topex-Poseidon dual-frequency radar altimeter observations over Boreal regions, *Int. J. Remote Sens.*, *27*, 4847–4866.

Papa, F., C. Prigent, F. Durand, and W. B. Rossow (2006b), Wetland dynamics using a suite of satellite observations: A case study of application and evaluation for the Indian Subcontinent, *Geophys. Res. Lett.*, *33*, L08401, doi:10.1029/2006GL025767.

Prigent, C., W. B. Rossow, and E. Matthews (1997), Microwave land surface emissivities estimated from SSM/I observations, *J. Geophys. Res.*, *102*, 21,867–21,890.

Prigent, C., E. Matthews, F. Aires, and W. B. Rossow (2001a), Remote sensing of global wetland dynamics with multiple satellite data sets, *Geophys. Res. Lett.*, *28*, 4631–4634.

Prigent, C., F. Aires, W. B. Rossow, and E. Matthews (2001b), Joint characterization of vegetation by satellite observations from visible to microwave wavelength: A sensitivity analysis, *J. Geophys. Res.*, *106*, 20,665–20,685.

Prigent, C., F. Aires, and W. B. Rossow (2006), Land surface microwave emissivities over the globe for a decade, *Bull. Am. Meteorol. Soc.*, *87*, 1573–1584, doi:10.1175/BAMS-87-11-1573.

Ramsar Convention (1971), The convention on wetlands of international importance especially as waterfowl habitat, UNESCO, Ramsar, Iran.

Richey, J. E., J. M. Melack, A. K. Aufdenkampe, V. M. Ballester, and L. Hess (2002), Outgassing from Amazonian rivers and wetlands as a large tropical source of atmospheric CO2, *Nature*, *416*, 617–620.

Reichhardt, T. (1995), Academy under fire on "wetlands" definition, *Nature*, *375*, 171.

Ropelewski, C. F., and M. S. Halpert (1987), Global and regional scale precipitation patterns associated with the El Nino/Southern Oscillation, *Mon. Weather Rev.*, *115*, 1606–1626.

Ropelewski, C. F., and M. S. Halpert (1989), Precipitation patterns associated with the high index phase of the Southern Oscillation, *J. Clim.*, *2*, 268–284.

Rossow, W. B., and L. C. Garder (1993), Cloud detection using satellite measurements of infrared and visible radiances for ISCCP, *J. Clim.*, *6*, 2341–2369, doi:10.1175/1520-0442.

Rossow, W. B., and R. A. Schiffer (1999), Advances in understanding clouds from ISCCP, *Bull. Am. Meteorol. Soc.*, *80*, 2261–2287.

Sahagian, D., and J. Melack (1996), Global wetland distribution and functional characterization: Trace gases and the hydrologic cycle, Wetlands Workshop Report, IGBP Workshop, Santa Barbara, Calif.

Shindell, D. T., G. Falugevi, N. Bell, and G. A. Schmidt (2004), An emission-based veiw of climate forcing by methane and tropospheric ozone, *Geophys. Res. Lett.*, *32*, L04803, doi:10.1029/2004GL021900.

Sippel, S. J., S. K. Hamilton, J. M. Melack, and E. M. M. Novo (1998), Passive microwave observations of inundation area and the area/stage relation in the Amazon River floodplain, *Int. J. Remote Sens.*, *19*, 3055–3074.

Walter, B. P., M. Heinman, and E. Matthews (2001a), Modeling modern methane emission from natural wetlands: 1. Model description and results, *J. Geophys. Res.*, *106*, 34,189–34,206.

Walter, B. P., M. Heinman, and E. Matthews (2001b), Modeling modern methane emission from natural wetlands: 2. Interannual variations 1982–1993, *J. Geophys. Res.*, *106*, 34,207–34,219.

Walter, K. M., S. A. Zimov, J. P. Chanton, D. Verbyla, and F. S. Chapin (2006), Methane bubbling from Siberian thaw lakes as a positive feedback to climate warming, *Nature*, *443*, 71–75.

Wielicki, B. A., and L. Parker (1992), On the determination of cloud cover from satellite sensors: The effect of sensor spatial resolution, *J. Geophys. Res.*, *97*, 12,799–12,823.

_____

F. Aires, CNRS/IPSL/Laboratoire de Météorologie Dynamique, IPSL, CNRS, Université Pierre et Marie Curie, 4, place Jussieu, F-75252 Paris Cédex 05, France. (filipe.aires@lmd.jussieu.fr)

E. Matthews and W. B. Rossow, NASA/GISS, 2880 New York, NY, 10025, USA. (ematthews@giss.nasa.gov; wrossow@giss.nasa.gov)

F. Papa, Columbia University, NASA/GISS, 2880 New York, NY, 10025, USA. (fpapa@giss.nasa.gov)

C. Prigent, CNRS, Laboratoire d'Etudes du Rayonnement et de la Matière en Astrophysique, Observatoire de Paris, 61, av. de l'Observatoire, F-75014 Paris, France. (catherine.prigent@obspm.fr)